Available online at www.sciencedirect.com
SCIENCE DIRECT®
Journal of Solid State Chemistry 175 (2003) 170–181
JOURNAL OF SOLID STATE CHEMISTRY
http://elsevier.com/locate/jssc

Phase equilibria, crystal structures, and dielectric anomaly in the $BaZrO_3$–$CaZrO_3$ system

Igor Levin,[a,*] Tammy G. Amos,[a] Steven M. Bell,[b] Leon Farber,[c] Terrell A. Vanderah,[a] Robert S. Roth,[a] and Brian H. Toby[a]

[a] *Materials Science and Engineering Laboratory, National Institute of Standards and Technology, Stop 8529, NIST, Gaithersburg, MD 20899, USA*
[b] *TRAK Ceramics, Inc., Hagerstown, MD, USA*
[c] *Department of Materials Science and Engineering, University of Pennsylvania, Philadelphia, PA, USA*

Received 3 March 2003; accepted 16 April 2003

Abstract

Phase equilibria in the $(1-x)BaZrO_3$–$xCaZrO_3$ system were analyzed using a combination of X-ray and neutron powder diffraction, and transmission electron microscopy. The proposed phase diagram features two extended two-phase fields containing mixtures of a Ba-rich cubic phase and a tetragonal, or orthorhombic Ca-rich phase, all having perovskite-related structures. The symmetry differences in the Ca-rich phases are caused by different tilting patterns of the $[ZrO_6]$ octahedra. In specimens quenched from 1650°C, $CaZrO_3$ dissolves only a few percent of Ba, whereas the solubility of Ca in $BaZrO_3$ is approximately 30 at%. The $BaZrO_3$–$CaZrO_3$ system features at least two tilting phase transitions, $Pm3m \rightarrow I4/mcm$ and $I4/mcm \rightarrow Pbnm$. Rietveld refinements of the $Ba_{0.8}Ca_{0.2}ZrO_3$ structure using variable-temperature neutron powder diffraction data confirmed that the $Pm3m \rightarrow I4/mcm$ transition corresponds to a rotation of octahedra about one of the cubic axes; successive octahedra along this axis rotate in opposite directions. In situ variable-temperature electron diffraction studies indicated that the transition temperature increases with increasing Ca-substitution on the *A*-sites, from approximately −120°C at 5 at% Ca to 225°C at 20 at% Ca. Dielectric measurements revealed that the permittivity increases monotonically from 36 for $BaZrO_3$ to 53 for $Ba_{0.9}Ca_{0.1}ZrO_3$, and then decreases to 50 for $Ba_{0.8}Ca_{0.2}ZrO_3$. This later specimen was the Ca-richest composition for which pellets could be quenched from the single-phase cubic field with presently available equipment. Strongly non-monotonic behavior was also observed for the temperature coefficient of resonant frequency; however, in this case, the maximum occurred at a lower Ca concentration, $0.05 \leqslant x \leqslant 0.1$. The non-linear behavior of the dielectric properties was attributed to two competing structural effects: a positive effect associated with substitution of relatively small Ca cations on the *A*-sites, resulting in stretched Ca–O bonds, and a negative effect, related to the distortion of the *A*-site environment (bond strain relaxation) upon octahedral tilting.

1. Introduction

Complex oxides with perovskite-like structures are attractive candidates for use in wireless communication applications, which require a combination of high permittivity (ε), near-zero temperature coefficient of the resonant frequency (τ_f), and low dielectric loss tangent ($\tan\delta$). Many recent studies of such oxide systems have focussed on the phase equilibria and dielectric properties of perovskite-related solid solutions having $CaTiO_3$, $SrTiO_3$ or $BaTiO_3$—all of which exhibit large permittivities—as one of the end-compounds [1–3]. In contrast, $AZrO_3$-based perovskites, which exhibit much lower permittivities than their titanate analogs, have received less attention. An interesting dielectric anomaly has been reported for the $CaZrO_3$(CZ)–$SrZrO_3$(SZ)–$BaZrO_3$(BZ) system: Yamaguchi et al. [4] observed that both ε and τ_f in the BZ–CZ system exhibit maxima at 20 mol% $CaZrO_3$; in contrast, these properties change monotonically between the end-compounds in the other two binary systems. Despite this anomalous difference in dielectric behavior between the BZ–CZ and both CZ–SZ and BZ–SZ ceramics, the detailed phase equilibria and structural behavior in the three systems have not been clarified.

The room-temperature crystal structures of all three end-compounds have been reported in the literature:

*Corresponding author. Fax: +301-975-5334.
E-mail address: igor.levin@nist.gov (I. Levin).

0022-4596/03/$ - see front matter © 2003 Elsevier Inc. All rights reserved.
doi:10.1016/S0022-4596(03)00220-2

$BaZrO_3$ crystallizes with an ideal cubic $Pm3m$ ($a = a_c$) perovskite structure [5], while both $CaZrO_3$ [6] and $SrZrO_3$ [7] exhibit orthorhombic $Pbnm$ ($\sqrt{2}a_c \times \sqrt{2}a_c \times 2a_c$) symmetry determined by rotation ($b^-b^-c^+$ type according to Glaezer's notation [8]) of the oxygen octahedra. Recently, Kennedy et al. [9] conducted a detailed analysis of tilting phase transitions in SZ–BZ perovskite solid solutions; however, no such studies have yet been reported for either the BZ–CZ or CZ–SZ systems. Yamaguchi et al. [4] presented some results on phase assemblages in the ternary CZ–BZ–SZ system. In particular, they reported the existence of cubic and orthorhombic perovskite solid solutions in the (Ba, Sr)-rich and (Sr, Ca)-rich regions, respectively, as well as their mixture in the (Ba, Ca)-rich part of the diagram; however, the results presented in that study were not sufficient to construct a phase diagram. In the present work, X-ray and neutron powder diffraction combined with transmission electron microscopy were applied to analyze phase equilibria and structural details in the BZ–CZ system, especially in regions associated with the dielectric anomaly. Dielectric properties were measured for selected compositions and correlated with the observed structural behavior.

2. Experiment

Polycrystalline samples in the $(1-x)BaZrO_3$–$xCaZrO_3$ system were prepared by solid state reaction of $CaCO_3$ (Alfa-Aesar,[1] 99.99%), $BaCO_3$ (Prochem Inc., 99.999%), and ZrO_2 (TAM, low Hf) powders. Stoichiometric amounts were first ground with acetone using an agate mortar and pestle. Mixtures were pressed into pellets and placed on beds of sacrificial powder of the same composition on Pt foil supported on alumina plates. After an overnight calcine at 950°C, multiple heatings (with intermediate grinding and repelletizing) were carried out at temperatures progressively increasing from 1400°C to 1550°C; samples were furnace-cooled to 700°C and then quenched on the bench top. Typically, four to six heatings were required to attain equilibrium, which was presumed when no further changes were observed in the details of the X-ray powder diffraction patterns. Specimens in welded Pt capsules were quenched in water from various temperatures (up to 1650°C) to further characterize phase equilibria in the system.

X-ray powder diffraction data were obtained using a Phillips diffractometer equipped with incident Soller slits, a theta-compensating divergence slit, graphite monochromator, and a scintillation detector. The patterns were collected at ambient temperatures using Cu$K\alpha$ radiation.

Neutron powder diffraction data for Rietveld analysis were collected on the BT-1 diffractometer at the Center for Neutron Research at the National Institute of Standards and Technology, using a Cu(311) monochromator with a wavelength of 1.5402(2) Å, and an array of 32 He-3 detectors at 5° intervals. Collimation of 15′, 20′, and 7′ arc were used before and after the monochromator, and after the sample, respectively. All samples were sealed under a He exchange gas in vanadium sample containers. Diffraction measurements were collected over a 2θ range of 3–168° with a step size of 0.05°. Closed-cycle He refrigerators were used for temperature control. The General Structure Analysis System (GSAS) software package was used for Rietveld structural refinements [10].

Specimens for transmission electron microscopy were prepared from sintered pellets by conventional grinding and polishing followed by mechanical dimpling to a thickness of 30 μm. The final thinning was accomplished in the Gatan Precision Ion-Polishing System (PIPS) at 5 kV and an angle of 5° until perforation. The specimens were examined using a Phillips 430 TEM operated at 200 kV. In situ variable-temperature studies were conducted between −173°C and 1000°C with double-tilt heating and cooling Gatan specimen holders.

Dielectric measurements were conducted on sintered pellets (approximately 12 mm diameter by 5 mm thick) using a cylindrical resonant cavity and an HP 8720D Vector Network Analyzer (VNA). Dielectric constants, ε, were calculated from the sample's size and the frequency of the $TE_{01\delta}$ resonance mode [11]. The measured dielectric constants were corrected to theoretical densities using a two-phase media formalism [12]; the typical uncertainty in the corrected values of ε is less than 5%. The unloaded quality factors were measured at ambient temperature using the transmission method with an estimated repeatability of 5%. The temperature coefficients of resonant frequency, τ_f, were measured for each sample between the two temperatures of 25°C and 60°C using gold-plated aluminum cavities and a Tenney environmental chamber. The repeatability of τ_f was estimated as 3 ppm/°C or better for the tested samples. Capacitance measurements were carried out at 1 MHz using sintered cylindrical pellets (diameters ~8 mm) machined to a height of about 1.5 mm. The capacitance was measured using an HP4284A precision LCR meter combined with a Delta Design 9023 temperature chamber. The measurements were conducted in the frequency range from 100 Hz to 1 MHz, while the temperature decreased from 180°C to −173°C with a cooling rate of 4°C/min.

[1] The identification of any commercial product or trade name does not imply endorsement or recommendation by the National Institute of Standards and Technology.

3. Results and discussion

3.1. Phase equilibria in the $(1-x)BaZrO_3$–$xCaZrO_3$ system

3.1.1. Ca solubility limit in $BaZrO_3$

X-ray powder diffraction analyses of $(1-x)BaZrO_3$–$xCaZrO_3$ specimens with $x = 0.05$, 0.1, 0.12, 0.2, 0.3, 0.4 and 0.5 were used to establish the $T(x)$ line separating a high-temperature Ba-rich cubic phase from a two-phase region containing orthorhombic $CaZrO_3$, as shown in Fig. 1. X-ray diffraction patterns for both the $x = 0.5$ and 0.4 specimens quenched from temperatures up to 1650°C could be indexed according to a mixture of orthorhombic $CaZrO_3$ and cubic $BaZrO_3$-like phases (Fig. 2); the results agree with those of Yamaguchi et al. [4]. In contrast, the $x = 0.3$ specimen quenched from 1650°C contained only a cubic phase, which when subsequently annealed at 1550°C again featured a two-phase mixture; the transformation was found to be reversible (Fig. 2).

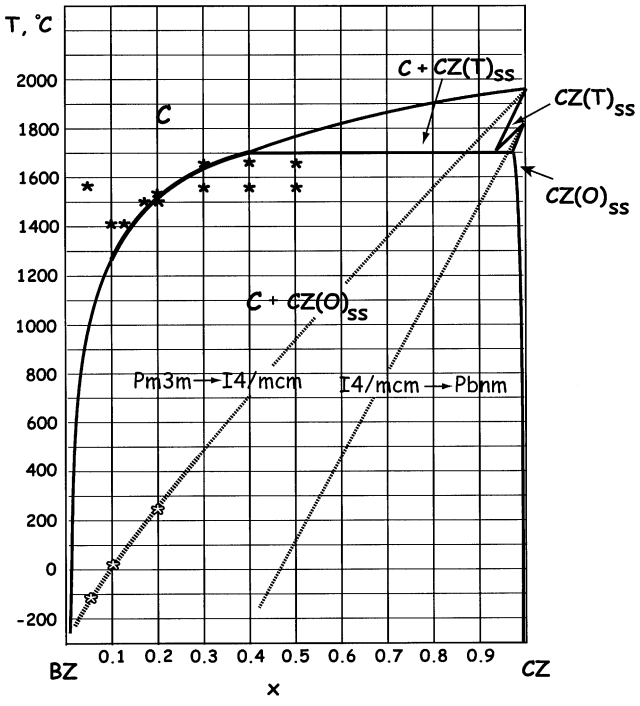

Fig. 1. Proposed phase diagram for the $(1-x)BaZrO_3$–$xCaZrO_3$ system. The solubility limit for Ca in cubic $BaZrO_3$ was determined using a series of annealing/quenching experiments (indicated using solid asterisks). The rest of the diagram is drawn based on the assumed temperatures of tilting phase transitions in $CaZrO_3$. The tilting phase transitions are indicated using dashed T_0-lines. The temperatures for the $C(Pm3m) \rightarrow T(I4/mcm)$ transition were estimated from in situ variable-temperature TEM studies for the three compositions, $x =$ 0.05, 0.10 and 0.20, as indicated by open asterisks. The $T(I4/mcm) \rightarrow O(Pbnm)$ transition temperature line is conjectural.

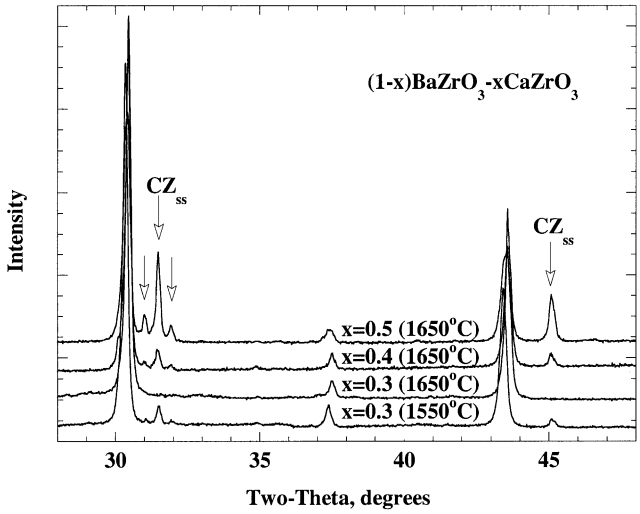

Fig. 2. Portions of the X-ray powder diffraction patterns for $(1-x)BZ : xCZ$ specimens. The patterns from the $x = 0.5$ and 0.4 specimens quenched from 1650°C can be indexed according to a mixture of cubic $BaZrO_3$-like and orthorhombic $CaZrO_3$-like phases; reflections unique for the $CaZrO_3$-like phase are indicated by arrows. The $x = 0.3$ specimen quenched from 1650°C contains only a $BaZrO_3$-like phase, while the same specimen annealed at 1550°C again features a two-phase mixture. Note that the amount of the $CaZrO_3$-like phase increases with increasing x.

3.1.2. Octahedral tilting phase transitions

Electron microscopy studies were conducted for the specimens with $x = 0$, 0.05, 0.1 and 0.2. The most detailed studies were carried out for the $x = 0.2$ sample, which represents the Ca-richest single-phase solid solution for which dense pellets could be obtained. Electron diffraction from grains in the $x = 0.2$ sample, air-quenched from the single-phase cubic field, revealed superlattice reflections at $\mathbf{k} = 1/2\langle 311 \rangle_c$ (where subscript 'c' refers to an ideal ~4 Å cubic perovskite unit cell). The existence of weak $\mathbf{k} = 1/2\langle 311 \rangle_c$-type reflections was further confirmed by X-ray and neutron powder diffraction; the reflections exhibited much stronger intensities with neutron radiation indicating that they originate from oxygen displacements. Tilting experiments in the electron microscope demonstrated that the $\mathbf{k} = 1/2\langle 111 \rangle_c$ reflections, which appear in the $\langle 110 \rangle_c$ zone axis diffraction patterns (Fig. 3), are extinct but exhibit non-zero intensity due to double diffraction on the $1/2\langle 311 \rangle_c$ reflections; these reflections were absent in the X-ray and neutron powder diffraction patterns. Each $\mathbf{k} = 1/2\langle 311 \rangle_c$ reflection featured streaks of diffuse intensity along the two (out of three) non-equivalent $\langle 001 \rangle_c$ directions (Fig. 3).

The reconstructed reciprocal lattice can be accounted for by the superposition of three tetragonal variants (having mutually perpendicular c-axis) with a $\sqrt{2}a_c \times \sqrt{2}a_c \times 2a_c$ unit cell and $I4/mcm$ symmetry. The presence of such fine-scale twin-related domains is evident from the dark-field images obtained using the

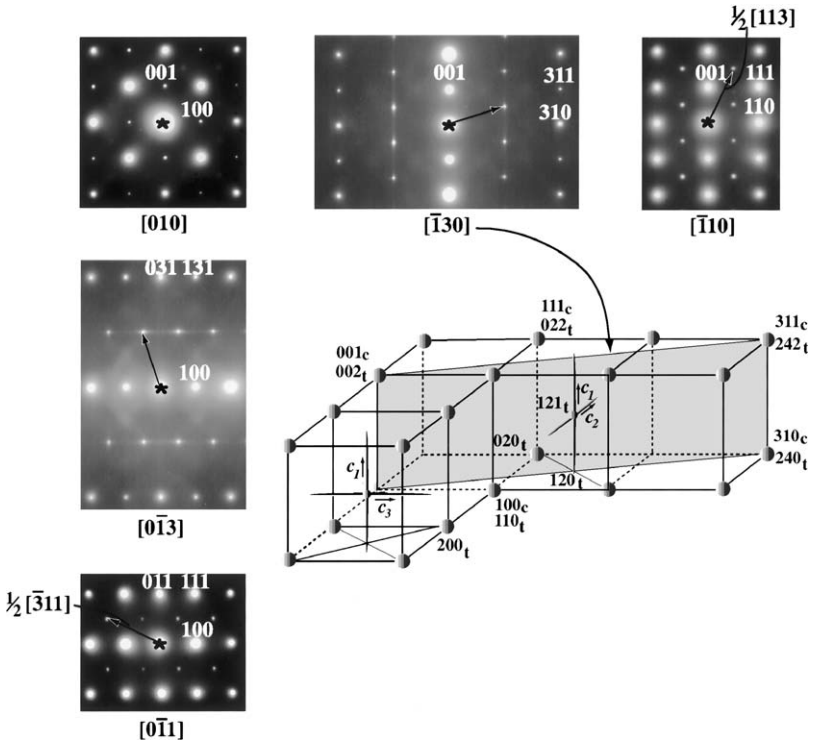

Fig. 3. Selected area electron diffraction patterns recorded from a single grain in the $x = 0.2$ specimen. The fundamental reflections are indexed according to a cubic ~4 Å unit cell. The $\langle 103 \rangle$ zone axis patterns feature $\mathbf{k} = 1/2\langle 113 \rangle$ type superlattice reflections. The 1/2[111]-type reflections in the $\langle 110 \rangle$ zone axes patterns arise due to double diffraction on the 1/2[311]-type reflections. The reconstructed reciprocal lattice can be indexed according to a tetragonal unit cell with the lattice parameters $a \approx \sqrt{2}a_c$ and $c = 2a_c$. The diffraction patterns additionally contain linear streaks of diffuse intensity passing through the superlattice reflections; each $1/2\langle 113 \rangle$ reflection exhibits two streaks directed along non-equivalent $\langle 100 \rangle$ directions.

$\mathbf{k} = 1/2\langle 311 \rangle_c$ reflections, strongly excited near the $\langle 103 \rangle_c$ orientation (Fig. 4); each $\mathbf{k} = 1/2\langle 311 \rangle_c$ reflection represents two of the three tetragonal variants. The size of the twin-related domains varied between different grains. The streaks of diffuse intensity through the $\mathbf{k} = 1/2\langle 311 \rangle_c$ reflections apparently originate from the high density of anti-phase boundaries having their normal approximately parallel to the corresponding c-axis (Fig. 5).

In situ variable-temperature TEM studies of the $x = 0.2$ sample demonstrated that the intensity of the $1/2\langle 311 \rangle_c$ reflections decreases gradually upon heating, becomes very diffuse at ~250°C, and vanishes completely at $T > 500$°C (Fig. 6). The observations are consistent with a displacive phase transition, which was confirmed to be reversible. Since the $1/2\langle 311 \rangle_c$ reflections arise from oxygen displacements, this transition was attributed to octahedral tilting. According to a symmetry classification of tilted perovskites [8,13], the tetragonal $\sqrt{2}a_c \times \sqrt{2}a_c \times 2a_c$ unit cell and $I4/mcm$ symmetry match an $a^0a^0c^-$-tilted structure, which is similar to the low-temperature form of $SrTiO_3$ [14]. No other phase transitions were observed for this composition down to −173°C. For the $x = 0.05$ and 0.10 specimens, a similar $Pm3m \rightarrow I4/mcm$ transition was observed to occur near −120°C and 20°C, respectively. For these two compositions, the superlattice reflections vanished within much narrower temperature ranges than for the $x = 0.2$ specimen, which reduced the uncertainty in the estimation of the transition temperature-composition line. The transition temperature varied somewhat among different grains (typically, three grains were analyzed in each specimen), presumably due to slight variations in the Ba/Ca ratio. In $BaZrO_3$, no phase transition was detected down to −173°C.

The anti-phase boundaries which produce streaks of diffuse intensity through the $\mathbf{k} = 1/2\langle 311 \rangle_c$ reflections, are attributed to a doubling of the c-lattice parameter accompanying the $Pm3m \rightarrow I4/mcm$ transition (Fig. 5); the octahedral tilting pattern at these boundaries is expected to change from $a^0a^0c^-$ to $a^0a^0c^+$. The density of anti-phase boundaries increases considerably as the transition temperature is approached, as evident from the preferential broadening of superlattice reflections along the c-axis. The relatively high incidence of such aligned anti-phase boundaries may be related to relatively high Ca-content on the A-sites; this interpretation is supported by the absence of detectable

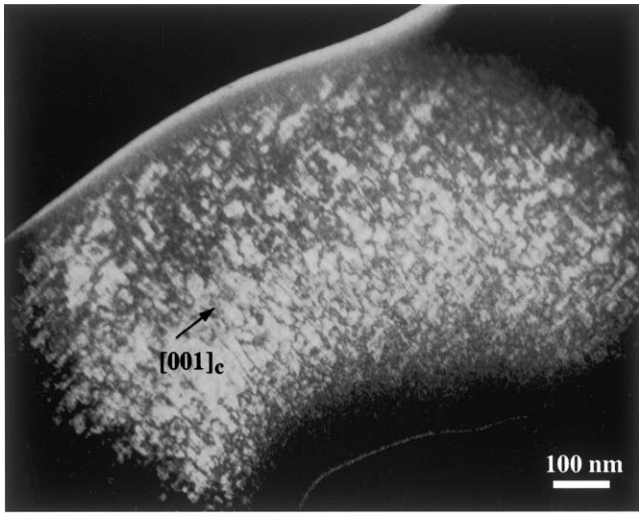

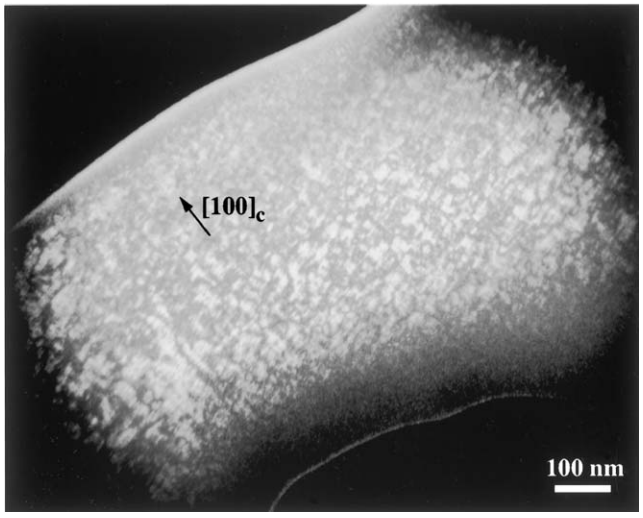

Fig. 4. Dark-field images of a single grain in the $x = 0.2$ specimen recorded with 1/2[113] (a) and 1/2[311] (b) reflections strongly excited near the $\langle 103 \rangle$ zone axis orientation. Each superlattice reflection represents two of the three twin-related tetragonal variants with perpendicular c-axis; these variants appear bright in the corresponding dark-field images. The images also feature fine striations aligned perpendicular to the $\langle 001 \rangle$ directions in each image. The striations were attributed to anti-phase boundaries resulting from the doubling of the unit cell upon the transition from cubic to tetragonal symmetry.

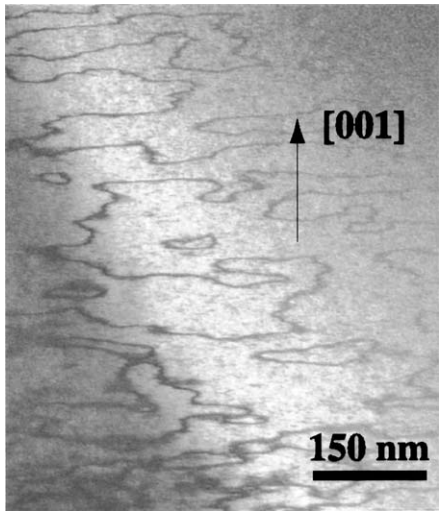

Fig. 5. Magnified dark-field image of a larger twin domain recorded with the 1/2[113] reflection strongly excited near the $\langle 103 \rangle$ zone axis orientation. The dark lines in the image correspond to the anti-phase boundaries associated with doubling of the cubic unit cell upon the cubic to tetragonal transition. The defect planes are aligned approximately perpendicular to the tetragonal c-axis. Octahedral tilting changes from $a^0a^0c^-$ inside a single domain to $a^0a^0c^+$ at the boundary plane.

streaking in the diffraction patterns of the tetragonal phase at composition $x = 0.05$.

Electron diffraction studies of the $x = 0.5$ specimen sintered at 1550°C revealed a mixture of grains of the orthorhombic (*Pbnm*) Ca-rich and tetragonal ($I4/mcm$) Ba-rich phases; both the reciprocal lattice and the domain microstructure of the tetragonal phase were similar to those observed in the $x = 0.2$ specimen. Furthermore, semi-quantitative compositional analysis using X-ray energy-dispersive spectroscopy in TEM (Fig. 7) confirmed that the tetragonal phases in both the $x = 0.5$ and 0.2 specimens exhibit similar compositions. Considering that the $Pm3m \rightarrow I4/mcm$ transition for the $x = 0.2$ composition occurs around 250°C, the equilibrium two-phase mixture at higher temperatures must contain a Ba-rich cubic phase and a Ca-rich phase having tetragonal or orthorhombic symmetry depending on the temperatures of the corresponding tilting phase transitions in $CaZrO_3$. Unfortunately, no details of the tilting phase transitions in $CaZrO_3$ have been reported, except for transition temperature of 1960°C between the tetragonal tilted and cubic untilted structures [15]. In $SrZrO_3$, the sequence of tilting phase transitions $a^0a^0a^0$ $(Pm3m) \rightarrow a^0a^0c^-(I4/mcm) \rightarrow b^-b^-a^0(Imma) \rightarrow b^-b^-c^+$ (*Pnma*) has been observed to occur between 1170°C and 700°C [7]. The driving force for octahedral tilting commonly increases with decreasing perovskite tolerance factor, $t = (R_A + R_O)/\sqrt{2}(R_B + R_O)$ [16]. Therefore, the temperatures of tilting phase transitions in $CaZrO_3$ ($t = 0.91$) are expected to be appreciably higher than those in $SrZrO_3$ ($t = 0.95$).

3.1.3. $BaZrO_3$–$CaZrO_3$ phase diagram

The schematic phase diagram proposed for the $BaZrO_3$–$CaZrO_3$ system is shown in Fig. 1; the diagram was drawn using the present experimental data and the assumed temperatures of tilting phase transitions in $CaZrO_3$. In addition to equilibrium phase reactions, the system features at least two displacive phase transitions: $Pm3m \rightarrow I4/mcm$ ($C \rightarrow T$) and $I4/mcm \rightarrow Pbnm$ ($T \rightarrow O$); the approximate T_0 lines for these transitions are shown using dashed lines. The T_0 line for the $Pm3m \rightarrow I4/mcm$ transition is drawn based on the observed transition temperatures for the $x = 0.05$, 0.1 and 0.2 compositions,

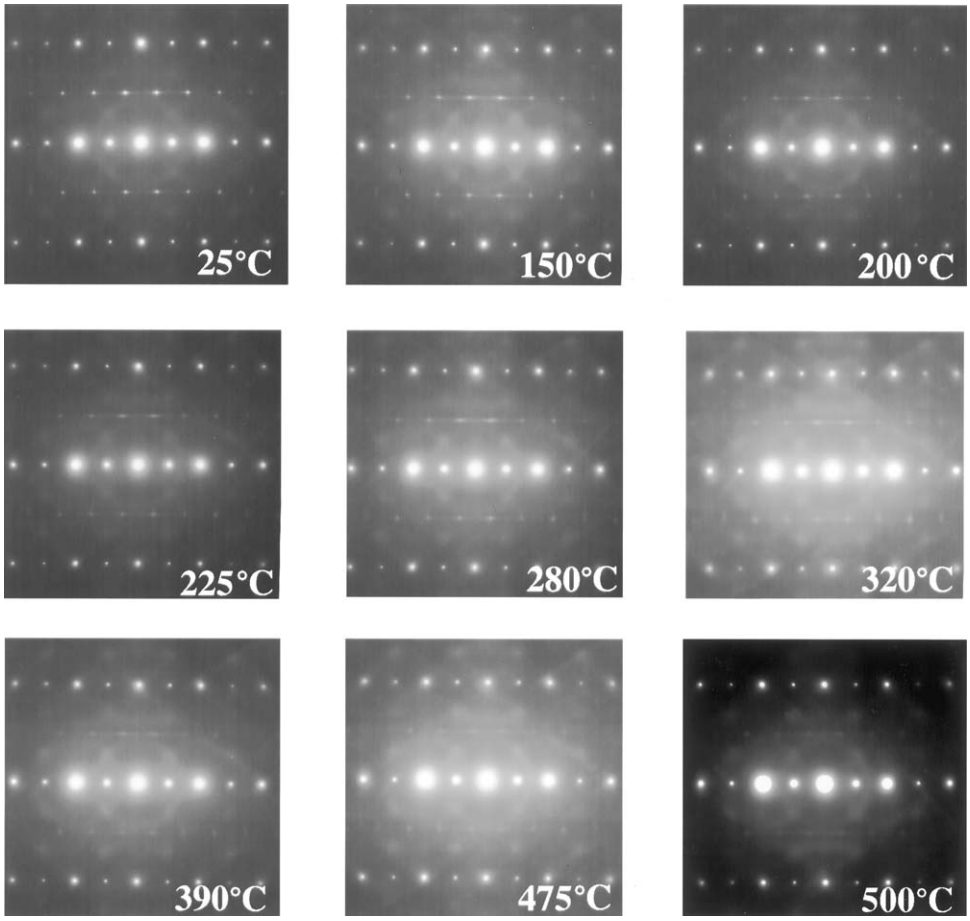

Fig. 6. Selected area electron diffraction patterns recorded at different temperatures from a single grain with $x = 0.2$ in the $\langle 103 \rangle$ cubic orientation. The intensity of the $1/2\langle 113 \rangle$ superlattice reflections decreases gradually with increasing temperature; these reflections become very weak and diffuse above $\sim$250°C, but still remain visible up to $\sim$500°C. The results manifest occurrence of a reversible displacive phase transition attributed to rotation of [BO_6] octahedra. The transition is broad, with an ill-defined transition temperature.

while the T_0 line for the $I4/mcm \rightarrow Pbnm$ transition is purely schematic. The grains of the Ca-rich phase in the $x = 0.5$ specimen synthesized at 1550°C contained very few twin domain boundaries, which suggests that the sintering took place in the $CZ_{ss}(O) + BZ_{ss}(C)$ phase field. Detailed analyses of the twin domain microstructures in the specimens annealed at different temperatures could help to establish the temperatures of the proposed phase reactions; however, these experiments were beyond the scope of the present study.

3.2. Rietveld refinements using neutron powder diffraction data

Structural refinements were carried out for $Ba_{0.8}Ca_{0.2}ZrO_3$ and for the end-member reference compounds $BaZrO_3$ and $CaZrO_3$. The initial parameters for the end-members were taken from Refs. [5,6], respectively, and datasets were collected at 173, 298, 373, and 473 K. Structural data for $BaZrO_3$ and $CaZrO_3$ are summarized in Tables 1 and 2; the refined lattice parameters for both compounds were in good agreement with the values from X-ray diffraction studies. For $BaZrO_3$, the bond valence sum (BVS) calculations [17] using the refined bond distances at $T =$ 298 K yielded 1.93 v.u. for Ba^{2+} and 3.89 v.u. for Zr^{4+}, which are close to the formal valences and suggest little or no bond strain. For the $CaZrO_3$ structure, the BVS value for Ca^{2+} at $T = 298$ K is equal to 1.79 v.u. (the coordination number of Ca is 8), indicating residual Ca–O bond tension.

Structural data for $Ba_{0.8}Ca_{0.2}ZrO_3$ are given in Table 3. At 450 K and below, the structure was refined in space group $I4/mcm$ with atoms located at the following positions: Ba and Ca: (4*b*) 0, 1/2, 1/4; Zr: (4*c*) 0, 0, 0; O1: (4*a*) 0, 0, 1/4: O2: (8*h*) x, $x + 1/2$, 0 (with $x \approx 0.25$). Because both Ba and Ca exhibit similar neutron coherent cross-sections ($b_{Ba} = 3.2 \times 10^{-24}$ cm^2, $b_{Ca} = 2.7 \times 10^{-24}$ cm^2), the occupancy factors for the mixed Ba/Ca sites were fixed at the nominal composition. Refined parameters included scale factor, background coefficients, profile coefficients, and

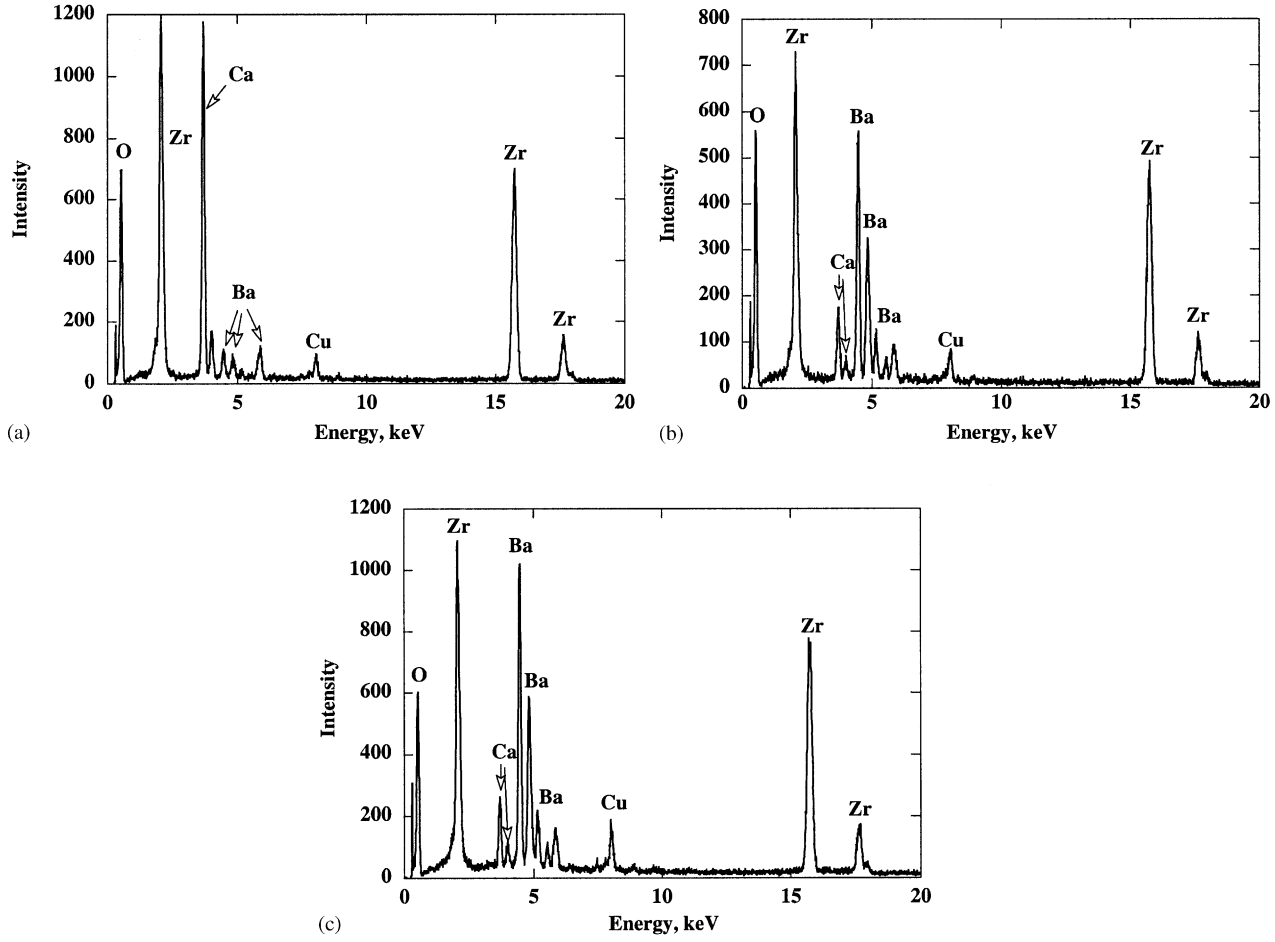

Fig. 7. EDS X-ray spectra recorded in TEM from adjacent (a) Ca-rich (orthorhombic) and (b) Ba-rich (tetragonal) grains, respectively, in the $x = 0.5$ specimen annealed at 1550°C. (c) EDS X-ray spectrum recorded from the $x = 0.2$ specimen. The Ba-rich tetragonal phases in both specimens feature similar chemical compositions in support of the diagram as drawn in Fig. 1.

Table 1
Variable-temperature structural parameters of $BaZrO_3$ (space group $Pm3m$) refined using neutron powder diffraction data

		T(K)			
		173	298	373	473
a (Å)		4.19134(4)	4.19430(6)	4.19603(4)	4.19880(5)
Ba (1b)	U_{11}	0.56(2)	0.86(2)	0.97(2)	1.21(2)
Zr (1a)	U_{11}	0.39(1)	0.58(2)	0.59(1)	0.75(1)
O (3d)	U_{11}	0.34(3)	0.42(2)	0.45(2)	0.52(3)
	U_{22}	0.97(2)	1.43(3)	1.61(2)	1.96(2)
Zr–O (Å)		2.09567(2)	2.09715(3)	2.09801(2)	2.0994(2)

The atom positional parameters are: Ba 1a (0,0,0), Zr 1b (1/2,1/2,1/2) and O 3c (0,1/2,1/2). Atomic thermal (displacement) parameters are $\times 100$ Å^2. The symmetry constraints on the thermal parameters in the $Pm3m$ space group are as following: for Ba and Zr $U_{11} = U_{22} = U_{33}$, $U_{12} = U_{13} = U_{23} = 0$; for O $U_{22} = U_{33}$, $U_{12} = U_{13} = U_{23} = 0$.

anisotropic thermal displacement parameters (with the Ba and Ca displacement parameters constrained to be equal). Also refined was the O2 x parameter, the only positional variable not constrained by symmetry. The refinements produced satisfactory agreement factors: $\chi^2 = 1.665$, $R_p = 4.98\%$, $R_{wp} = 6.48\%$ for 2599 observations and 42 variables (Fig. 8); similar fitting statistics were obtained for all temperatures from 20 to 450 K. The refined positional parameters confirm that in this temperature range the structure features $a^0a^0c^-$ octahedral tilting (Fig. 9). The tilting angle, calculated from the refined x parameter for the O2 atoms, decreases with

Table 2
Variable-temperature structural parameters for $CaZrO_3$

		T(K)			
		173	298	373	473
a (Å)		5.58305(7)	5.59111(7)	5.59380(7)	5.59998(7)
b (Å)		8.00703(11)	8.01687(11)	8.01984(11)	8.02700(11)
c (Å)		5.75904(7)	5.76128(8)	5.76115(8)	5.76268(8)
Ca (4c)	x	0.0122(2)	0.0125(2)	0.0117(2)	0.0114(2)
	z	0.0495(1)	0.0485(2)	0.0483(2)	0.0473(2)
	U_{11}	0.71(4)	0.88(5)	1.19(5)	1.37(5)
	U_{22}	0.97(5)	1.15(5)	1.35(5)	1.59(6)
	U_{33}	0.78(4)	1.15(4)	1.29(4)	1.55(4)
	U_{13}	0.02(4)	0.02(4)	−0.09(5)	0.00(5)
Zr (4b)	U_{11}	0.46(3)	0.46(3)	0.63(3)	0.75(3)
	U_{22}	0.43(3)	0.55(3)	0.63(3)	0.78(3)
	U_{33}	0.42(3)	0.53(3)	0.60(3)	0.66(3)
	U_{12}	0.05(3)	0.06(3)	0.08(3)	0.05(3)
	U_{13}	−0.05(3)	0.00(3)	−0.02(3)	−0.05(3)
	U_{23}	0.02(2)	0.06(2)	0.05(2)	0.08(2)
O1 (4c)	x	0.6044(2)	0.6036(2)	0.6030(1)	0.6023(2)
	z	−0.0401(1)	−0.0397(1)	−0.0394(1)	−0.0389(1)
	U_{11}	0.58(4)	0.77(4)	0.90(4)	1.15(4)
	U_{22}	0.42(3)	0.42(4)	0.52(4)	0.46(4)
	U_{33}	0.66(4)	0.94(4)	1.17(4)	1.43(4)
	U_{13}	−0.04(3)	−0.07(4)	−0.04(3)	−0.04(4)
O2 (8d)	x	0.3024(1)	0.3022(1)	0.3022(1)	0.3021(1)
	y	0.0554(1)	0.0546(1)	0.0543(1)	0.0539(1)
	z	0.3000(1)	0.3000(1)	0.3000(1)	0.2999(1)
	U_{11}	0.59(3)	0.76(3)	0.92(3)	1.13(3)
	U_{22}	0.68(3)	0.93(3)	1.16(3)	1.40(3)
	U_{33}	0.56(3)	0.73(3)	0.82(3)	0.99(3)
	U_{12}	−0.09(2)	0.13(2)	−0.18(2)	−0.21(3)
	U_{13}	0.21(2)	0.30(3)	0.39(3)	0.44(3)
	U_{23}	−0.15(2)	−0.22(2)	−0.24(2)	−0.27(2)
Zr–O1 (Å)		2.09779(3)	2.09893(3)	2.09846(3)	2.09896(3)
Zr–O2 (Å)		2.0977(6)	2.0984(6)	2.0980(6)	2.0987(6)
Zr–O2 (Å)		2.0911(5)	2.0913(6)	2.0916(5)	2.0924(6)

Space group is *Pcmn* (#62). The atoms occupy the following Wyckoff positions: Ca 4c (x 1/4 z), Zr 4b (001/2), O 4c (x 1/4 z), 8d (x y z). Atomic thermal (displacement) parameters are $\times 100$ Å^2. The Thermal parameters for both Ca and O1 are constrained by symmetry as $U_{12} = U_{23} = 0$.

increasing temperature from 3.6° at 20 K to 1.1° at 450 K (Table 3, Fig. 10). A reversible phase transition to the untilted cubic *Pm*3*m* structure was observed between 450 K (177°C) and 500 K (227°C), as inferred from the disappearance of the superlattice reflections. Therefore, the refinements at both 500 and 675 K were based on the $BaZrO_3$ cubic structure with 20% Ca substitution on the Ba sites. The transition temperature deduced using neutron diffraction data is similar to that at which significant weakening and broadening of the superlattice reflections occurred in the electron diffraction patterns. The diffuse superstructure reflections observed by electron diffraction up to ~500°C were apparently below the detection limit for the neutron powder diffraction data. The microscopic heterogeneities in the Ba/Ca ratio (which could cause appreciable variation of T_0, Fig. 1) could also contribute to the discrepancy between the results of neutron diffraction and TEM, because of the limited sampling in the latter analysis.

In addition to octahedral tilting, the tetragonal structure of $Ba_{0.8}Ca_{0.2}ZrO_3$ features weak distortions of the [ZrO_6] octahedra at lower temperatures: The octahedra are slightly compressed in the z direction, with shorter axial Zr–O1 bond distances, as seen in Table 3. The distortion is most dramatic at 20 K, with a Zr–O1 bond distance of 2.0843(1) Å and Zr–O2 of 2.0879(2) Å, a difference of 0.0036 Å. As the temperature increases, the equatorial Zr–O2 bond distance remains fairly constant, while the axial Zr–O1 distance increases. The Zr–O2–Zr bond angle is 170° at 20 K and gradually approaches 180° with increasing temperature. The thermal ellipsoids for Zr at temperatures $T < 298$ K are significantly elongated along the c-axis, while these become nearly isotropic at $T > 375$ K. This anisotropy in the displacement parameters suggests

Table 3
Selected structural features for $Ba_{0.8}Ca_{0.2}ZrO_3$

		T(K)						
		20	173	298	375	450	500	675
a (Å)		5.8824(2)	5.8864(1)	5.8938(1)	5.8987(2)	5.9031(1)	4.1770(1)	4.1827(1)
c (Å)		8.3372(3)	8.3416(3)	8.3459(2)	8.3534(3)	8.3585(3)		
O2 x		0.2277(3)	0.2293(2)	0.2341(2)	0.2395(3)	0.2432(3)	0.25	0.25
Tilt angle (°)		3.60	3.35	2.57	1.70	1.10	0	0
Zr–O1 (Å)		2.0843(1)	2.0854(1)	2.0864(1)	2.0883(1)	2.0896(1)	2.0885(1)	2.0914(1)
Zr–O2 (Å)		2.0879(2)	2.0882(2)	2.0879(1)	2.0873(1)	2.0878(1)		
Zr–O2–Zr (°)		169.8(1)	170.5(1)	172.7(1)	175.2(1)	176.9(2)	180(1)	180(1)
Ba/Ca	U_{11}	0.55(8)	0.81(7)	1.16(7)	1.40(9)	1.52(10)	1.67(3)	2.07(3)
	U_{33}	0.98(16)	1.13(15)	1.45(15)	0.99(18)	1.22(20)		
Zr	U_{11}	0.12(7)	0.27(6)	0.27(6)	0.54(8)	0.44(8)	0.76(3)	0.90(2)
	U_{33}	0.76(14)	0.66(13)	1.14(13)	0.27(16)	0.66(18)		
O1	U_{11}	3.33(18)	3.06(15)	3.50(16)	3.91(27)	3.12(24)	0.62(5)	0.74(4)
	U_{33}	0.06(15)	0.00(13)	0.22(15)	0.19(1)	−0.21(19)	3.56(5)	3.74(4)
O2	U_{11}	0.97(6)	1.27(6)	1.61(6)	1.81(13)	2.27(15)		
	U_{33}	2.88(15)	2.75(14)	2.89(15)	2.15(17)	2.69(20)		
	U_{32}	0.54(7)	0.79(7)	1.03(8)	1.36(14)	1.59(16)		

For $T \leqslant 450$ K the structure was refined in space group $I4/mcm$ (#140) with atoms located in the following positions: Ba/Ca 4*b* (0 1/2 1/4), Zr 4*c* (0 0 0), O1 4*a* (0 0 1/4), O2 8*h* ($x\,x+1/2\,0$). Atomic thermal (displacement) parameters are $\times 100$ Å^2. The thermal parameters are constrained by symmetry as follows: Ba/Ca, Zr, and O1: $U_{11}=U_{22}$, $U_{12}=U_{13}=U_{23}=0$; O2; $U_{11}=U_{22}$, $U_{13}=U_{23}=0$. Above 450 K, the structure was refined in space group $Pm3m$, with the thermal parameters constrained as: Ba/Ca, Zr $U_{11}=U_{22}=U_{33}$, $U_{12}=U_{13}=U_{23}=0$; O; $U_{22}=U_{33}$, $U_{12}=U_{13}=U_{23}=0$.

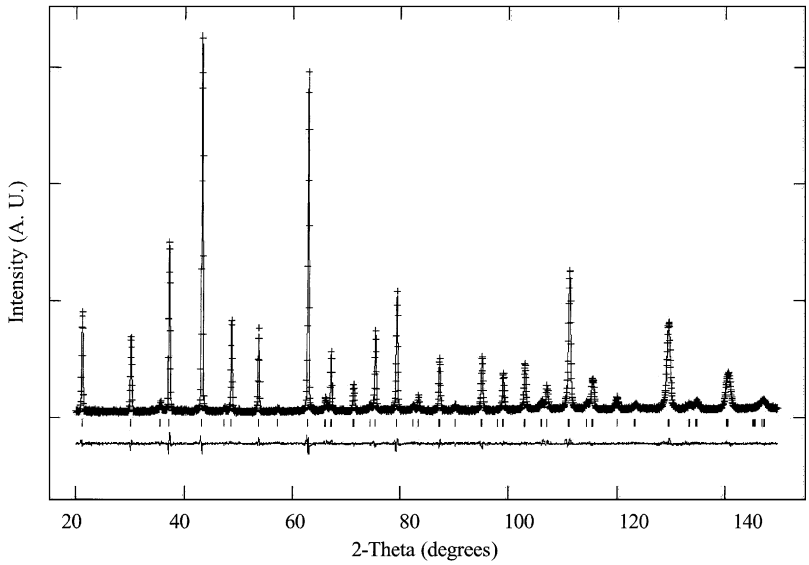

Fig. 8. Upper: Experimental (crosses) and calculated (line) neutron powder diffraction profiles for $Ba_{0.8}Ca_{0.2}ZrO_3$ ($T = 298$ K). Lower: Residual.

possible off-center Zr-displacements along the *c*-direction at low temperatures.

The thermal ellipsoids for the oxygen atoms at all temperatures up to a $I4/mcm \rightarrow Pm3m$ transition are strongly flattened and feature abnormally large values of displacement parameters (0.03 Å^2) in the directions perpendicular to the B–O bonds; the magnitudes of the atomic displacements remain similar for all temperatures. These results suggest appreciable static displacements of the oxygen atoms from their ideal positions in the $I4/mcm$ structure. The directions of these static displacements are consistent with local tilting of $[ZrO_6]$ octahedra superimposed onto the average $a^0a^0c^-$ tilting pattern. This local tilting is either disordered or exhibits short-range correlations only, and can be attributed to the size mismatch between Ba and Ca (~0.3 Å [18]) mixed on the *A*-sites; likely, the displacements of the oxygen atoms are related to the local distribution of Ba and Ca. The anti-phase boundaries, where the tilting pattern changes locally

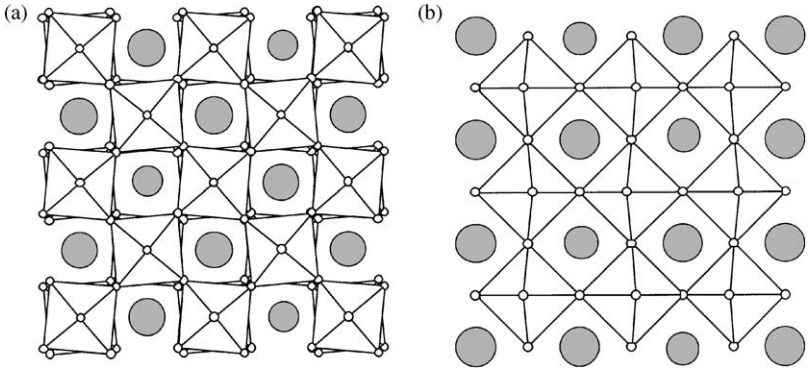

Fig. 9. Schematic projections of the $Ba_{0.8}Ca_{0.2}ZrO_3$ structure at 20 K along the (a) [001] and (b) [110] directions. Shaded circles represent *A*-cations, open circles oxygen; Zr cations occupy the octahedra.

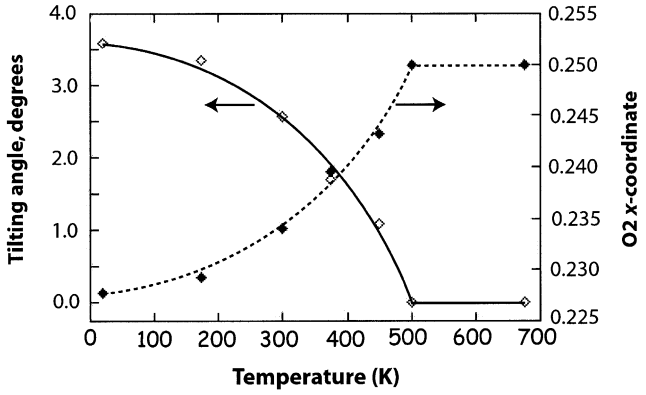

Fig. 10. Temperature dependence of the tilting angle for the $[ZrO_6]$ octahedra (open markers) and O2 *x*-coordinate (solid markers) in the $Ba_{0.8}Ca_{0.2}ZrO_3$ structure, as refined using neutron powder diffraction (Table 3). A reversible phase transition to the untilted cubic structure occurs between 450 and 500 K.

from $a^0a^0c^-$ to $a^0a^0c^+$, could also contribute to the abnormal displacement parameters of the oxygen atoms.

The (Ba/Ca)–O bonds in the $Ba_{0.8}Ca_{0.2}ZrO_3$ specimen exhibit appreciable residual tension: The bond valence sums for the mixed Ba/Ca sites are 1.80 and 1.77 v.u. at $T = 20$ and 298 K, respectively, which is similar to the value of 1.79 v.u. obtained for eight-fold coordinated Ca in $CaZrO_3$ at $T = 298$ K. In contrast to $CaZrO_3$, the first coordination sphere for the *A*-cations in $Ba_{0.8}Ca_{0.2}ZrO_3$ structure includes all 12 oxygen ions.

3.3. Dielectric properties

The results of our dielectric measurements at frequencies above 1 GHz for single-phase $Ba_{1-x}Ca_xZrO_3$ samples are listed in Table 4, and are in fair agreement with those reported by Yamaguchi et al. [4]. As Ca is substituted for Ba, the dielectric constant (ε) increases monotonically from 36 for $x = 0$ to 53 for $x = 0.1$, but then decreases to 50 for $x = 0.2$. However, the difference between the values of 53 and 50 is within the uncertainty of the present measurements. The temperature coefficient of resonant frequency (τ_f), exhibits a dramatic increase from +133 ppm/°C to +453 ppm/°C upon addition of only 5 at% Ca ($x = 0.05$), remains approximately constant up to $x = 0.1$, but decreases significantly to +179 ppm/°C for $x = 0.2$. Very similar trends were observed in variable-temperature capacitance measurements at 1 MHz (Fig. 11). Capacitance measurements between −170°C and 180°C for the $x = 0.05$ and 0.1 specimens revealed no features which could be associated with the tilting phase transitions known to occur in this temperature range. Such behavior may be attributed, at least partly, to compositional heterogeneities in the solid solutions which would smear broad and weak $\varepsilon(T)$ maxima typically associated with tilting transitions.

A continuous drop in both ε and τ_f with Ca content increasing beyond $x = 0.2$, as reported in Ref. [4], is caused by the increasing volume fraction of $CaZrO_3$ in these two-phase specimens (Figs. 1 and 2). Assuming that one could obtain single-phase specimens in the entire compositional range by quenching from the high-temperature *C* phase-field, we still expect to obtain an $\varepsilon(x)$ dependence with a maximum, because the permittivity of $CaZrO_3$ is lower than that measured for the single-phase $x = 0.2$ specimen (Table 4). According to our results, the maximum permittivity occurs between $x = 0.1$ and 0.2; that is, where the T_0 for the tilting transition crosses room temperature. Similar compositional dependences of permittivity have been reported for $Ba_{1-x}Sr_x(Mg_{1/3}Ta_{2/3})O_3$ solid solutions [19], and for several other complex perovskite systems with Ba/Ca and Ba/Sr mixtures on the *A*-sites [20]. The non-monotonic compositional dependence of dielectric constant suggests the existence of at least two competitive effects associated with the mixing of different cations on the *A*-sites. Since the permittivity increases monotonically with Ca-content for cubic $Ba_{1-x}Ca_xZrO_3$ solid solutions ($0 \leqslant x \leqslant 0.1$), these two effects can be intuitively identified as (i) a positive effect of Ca substitution

Table 4
Dielectric properties for single-phase $Ba_{1-x}Ca_xZrO_3$ specimens

Sample	ε		τ_f (ppm/°C)		Q	
	This work	Ref. [4]	This work	Ref. [4]	This work	Ref. [4] (at 11 GHz)
$BaZrO_3$	36	35.4	+133	+134	1800 at 4.8 GHz	800
$Ba_{0.95}Ca_{0.05}ZrO_3$	42	—	+453	—	880 at 4.8 GHz	—
$Ba_{0.9}Ca_{0.1}ZrO_3$	53	—	+458	—	430 at 4.1 GHz	—
$Ba_{0.8}Ca_{0.2}ZrO_3$	50	51.1	+179	+260	400 at 4.1 GHz	750
$CaZrO_3$	30	30.5	−26.5	+6	3100 at 5.6 GHz	2400

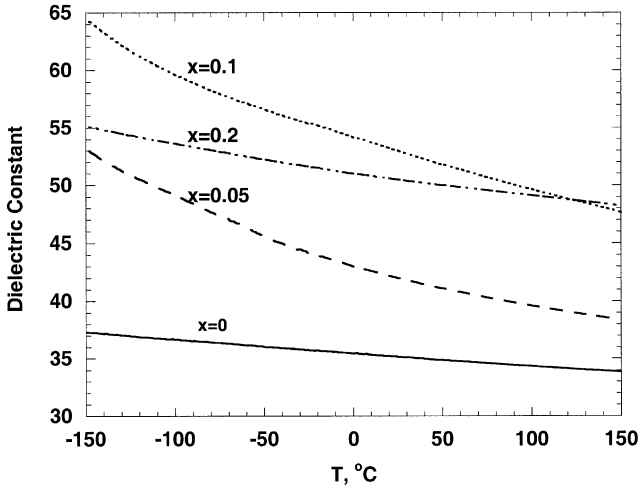

Fig. 11. Temperature dependence of the dielectric constant for single-phase $(1-x)BZ:xCZ$ specimens measured capacitively at 1 MHz. The results demonstrate clearly that both the relative permittivity and its temperature coefficient exhibit compositional maxima. Note the marked increase in τ_ε upon addition of only 5 at% Ca, which is similar to the temperature dependence of the 10 at% Ca specimen. At 20 at% Ca, the dependence reverts to resembling that of pure $BaZrO_3$.

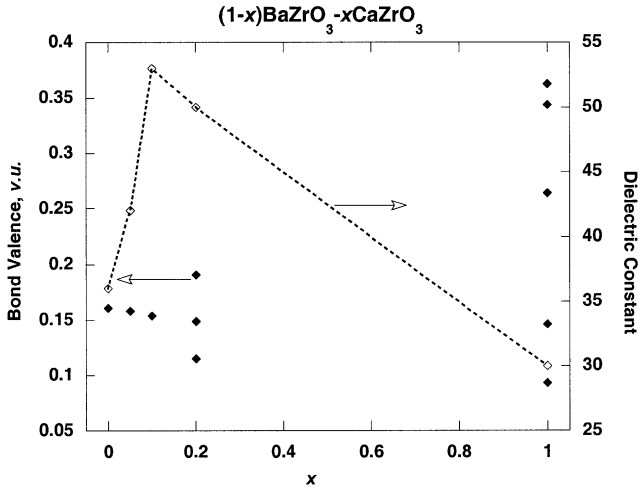

Fig. 12. Compositional dependence of A–O bond valences (solid markers) and dielectric constant (open markers) in the $Ba_{1-x}Ca_xZrO_3$ solid solutions. Bond valences were first calculated for the Ba and Ca separately using refined (Ba/Ca)–O bond distances, and then averaged according to the appropriate Ba/Ca ratios. The bond valences corresponding to distinct A–O bond distances only are shown in the plot (note that a cubic perovskite structure features 12 equivalent A–O bond distances).

resulting from stretched Ca–O bonds, and (ii) a negative effect caused by distortion of the A-site environment (accompanied by shortening of some A–O bonds) upon octahedral tilting. In fact, softening of the A–O bonds with increasing Ca-content in the cubic $Ba_{1-x}Ca_xZrO_3$ solid solutions is evident from the plot of A–O bond valences calculated using refined bond distances (Fig. 12). Octahedral tilting, which for $x = 0.2$ develops well above room-temperature, stiffens some of the A–O bonds.

As seen in Table 4, the magnitude of τ_f (or τ_ε in Fig. 11) for $BaZrO_3$ more than triples as Ca is substituted, reaching a maximum between $x = 0.05$ and 0.1. This remarkable increase cannot be accounted for by 17% increase in the permittivity. Such strong changes in the magnitude of τ_f with composition in perovskites are often associated with the onset of octahedral tilting [21,22]; however, the tilting phase transition for the $x = 0.05$ structure occurs well below room temperature ($T_0 \approx -120$°C) and, therefore cannot cause the observed changes in τ_f. The dramatic increase in τ_f with Ca concentration does correlate with the residual bond strain created by introducing relatively small Ca into the $BaZrO_3$ structure. Interpretation of τ_ε based on the analysis of Clausius–Mossotti equation [22] suggests that Ca substitution strongly enhances the anharmonicity of certain low-frequency polar vibration modes. A similar τ_f effect upon substitution of a smaller A-cation in the cubic perovskite structure has been reported previously [23]. The subsequent drop in τ_f for the $x = 0.2$ sample could be attributed to octahedral tilting (bond strain relaxation), which for this composition evolves at $T \approx 225$°C. Following these arguments, similar, though much weaker compositional maxima may also occur in the dielectric properties of $Ba_{1-x}Sr_xZrO_3$ solid-solutions which, unlike the $Ba_{1-x}Ca_xZrO_3$ system, encompass the entire compositional range. Surprisingly, Yamaguchi et al. [4] observed a monotonic change of dielectric properties in the $Ba_{1-x}Sr_xZrO_3$ system, though no properties have yet

been reported for $0<x<0.2$. Ab-initio calculations of dielectric properties for the $Ba_{1-x}Ca_xZrO_3$ system combined with far-infrared studies of polar vibrational modes are planned to clarify the exact origin of the non-monotonic compositional dependence.

4. Conclusions

Phase equilibria in the $(1-x)BaZrO_3$–$xCaZrO_3$ system were investigated using a combination of transmission electron microscopy with X-ray and neutron powder diffraction. The equilibrium phase diagram for this system features extended two-phase fields representing mixtures of a cubic Ba-rich phase and a tetragonal, or orthorhombic (in order of decreasing temperature), Ca-rich phase; all phases crystallize with perovskite-related structures. As expected, the solubility of Ba in $CaZrO_3$ is limited to a few percent in samples prepared at 1650°C, while the solubility of Ca in $BaZrO_3$ increases from a few percent at 1400°C to about 30% at 1650°C. The system features at least two octahedral tilting phase transitions $C(Pm3m)\rightarrow T(I4/mcm)$ and $T(I4/mcm)\rightarrow O(Pbnm)$ with the corresponding transition temperatures decreasing from $CaZrO_3$ to $BaZrO_3$. Rietveld refinements using variable-temperature neutron powder diffraction data for single-phase $Ba_{0.8}Ca_{0.2}ZrO_3$ confirmed that the $C\rightarrow T$ transition is associated with the $a^0a^0a^0\rightarrow a^0a^0c^-$ octahedral tilting transition, occurring near 225°C. The transition temperature was observed to decrease to $T\approx -120$°C for $x=0.05$. The refinements revealed significant local displacements of oxygen atoms from their special positions in the $I4/mcm$ space group, which were attributed to the apparent disorder of Ba and Ca cations on the A-sites. Dielectric measurements for single-phase $Ba_{1-x}Ca_xZrO_3$ samples revealed non-monotonic compositional dependences with maxima for both ε and τ_f, suggesting the coexistence of competitive effects on properties. We attributed the positive effect on the magnitude of both ε and τ_f to the size mismatch between Ba and Ca, which creates stretched Ca–O bonds, and the negative effect to distortion of the A-cation environment associated with octahedral tilting.

References

[1] J.H. Yang, C.K. Choo, W.K. Choo, Ferroelectrics 223 (1–4) (1999) 329–336.
[2] S. Kucheiko, J.W. Cho, H.J. Kim, H.J. Jung, J. Am. Ceram. Soc. 79 (10) (1996) 2739–2743.
[3] I. Levin, Y.J. Chan, S.M. Bell, J.E. Maslar, T.A. Vanderah, J. Appl. Phys. 90 (2) (2001) 904–914.
[4] T. Yamaguchi, Y. Komatsu, T. Otobe, Y. Murakami, Ferroelectrics 27 (1980) 273.
[5] H.D. Megaw, Proc. Phys. Soc. London 58 (1946) 133.
[6] H.J.A. Koopmans, G.M.H. van de Velde, P.J. Gellings, Acta Crystallogr. Sect. C 39 (1983) 133.
[7] B.J. Kennedy, C.J. Howard, B.C. Chakoumkos, Phys. Rev. B 59 (6) (1999) 4023.
[8] A.M. Glazer, Acta Crystallogr. Sect. C 28 (1972) 3384.
[9] B.J. Kennedy, C.J. Howard, G.J. Thorogood, J.R. Hester, J. Solid State Chem. 161 (2002) 106–112.
[10] A.C. Larson, R.B. Von Dreele, General Structure Analysis System, Report LAUR 86-748, Los Alamos National Laboratory, NM, 1994.
[11] D. Kajfez, P. Guillon, Dielectric Resonators, Artech House, Norwood, MA, 1987.
[12] R.G. Geyer, J. Baker-Jarvis, T.A. Vanderah, J. Mantese, Adv. Dielectr. Ceram. Mater. 88, 115–129.
[13] P.M. Woodward, Acta Crystallogr. B 53 (1997) 32–43.
[14] H. Thomas, K.A. Muller, Phys. Rev. Lett. 21 (1968) 1256.
[15] B.C. Chakoumakos, S.E. Nagler, S.T. Misture, H.M. Christen, Physica B 241 358.
[16] H.D. Megaw, Crystal Structures: A Working Approach, W.B. Saunders, Philadelphia, 1973.
[17] N.E. Brese, M. O'Keeffe, Acta Crystallogr. B 47 (1991) 192–197.
[18] R.D. Shannon, Acta Crystallogr. Sect. A 32 (1976) 751.
[19] T. Nagai, M. Sugiyama, M. Sando, K. Niihara, Jpn. J. Appl. Phys. 38 (1999) 822.
[20] H. Ikawa, M. Takemoto, Presented at the meeting on Microwave Materials and their Applications, September, 2002.
[21] I.M. Reaney, E.L. Colla, N. Setter, Jpn. J. Appl. Phys. 33 (1994) 3984–3990.
[22] P.J. Harrop, J. Mater. Sci. 4 (1969) 370.
[23] E.L. Colla, I.M. Reaney, N. Setter, J. Appl. Phys. 74 (5) (1993) 3414–3425.